Induced seismicity at the UK 'hot dry rock' test site for geothermal energy production

Xun Li,[1] Ian Main[2] and Andrew Jupe[3]

[1]*Center for Wave Phenomena, Colorado School of Mines,* 924 16th *Street, Golden, Colorado 80401, USA. Email:* lixun@mymail.mines.edu
[2]*School of GeoSciences, University of Edinburgh, James Hutton Road, Edinburgh EH9 3FE, UK*
[3]*Altcom Ltd,* 13 *North Parade, Penzance, Cornwall TR18 4SH, UK*

SUMMARY

In enhanced geothermal systems (EGS), fluid is injected at high pressure in order to stimulate fracturing and/or fluid flow through otherwise relatively impermeable underlying hot rocks to generate power and/or heat. The stimulation induces microearthquakes whose precise triggering mechanism and relationship to new and pre-existing fracture networks are still the subject of some debate. Here, we analyse the data set for induced microearthquakes at the UK 'hot dry rock' experimental geothermal site (Rosemanowes, Cornwall). We quantify the evolution of several metrics used to characterise induced seismicity, including the seismic strain partition factor and the 'seismogenic index'. The results show a low strain partition factor of 0.01 per cent and a low seismogenic index indicating that aseismic processes dominate. We also analyse the spatio-temporal distribution of hypocentres, using simple models for the evolution of hydraulic diffusivity by (1) isotropic and (2) anisotropic pore-pressure relaxation. The principal axes of the diffusivity or permeability tensor inferred from the spatial distribution of earthquake foci are aligned parallel to the present-day stress field, although the maximum permeability is vertical, whereas the maximum principal stress is horizontal. Our results are consistent with a triggering mechanism that involves (1) seismic shear slip along optimally oriented pre-existing fractures, (2) a large component of aseismic slip with creep and (3) activation of tensile fractures as hydraulic conduits created by both the present-day stress field and by the induced shear slip, both exploiting pre-existing joint sets exposed in borehole data.

Key words: Induced seismicity; Hydrothermal systems; Fracture and flow.

1 INTRODUCTION

Geothermal reservoirs at 'hot dry rock' sites around the world provide a significant potential and actual source of heat and/or electrical power (e.g. Oppenheimer 1986; Majer *et al.* 2007; Charléty *et al.* 2007; Ellsworth 2013; Schmittbuhl *et al.* 2014; Zang *et al.* 2014). This potential is commonly assessed and exploited by drilling boreholes for injection and production of fluid at a depth of at least 2 km into a layer of relatively low porosity and permeability host rock with an *in situ* temperature typically above 100 °C. In Enhanced Geothermal Systems (EGSs), fluid is injected at elevated pressure in order to stimulate fluid flow along pre-existing channels, or to create new ones deliberately by hydraulic fracture. The resulting elevated fluid pressures enhance porosity (and hence fluid storage) as well as permeability of reservoirs. In turn, the effective stress changes associated with injection can induce seismicity—not only directly by promoting tensile hydraulic fracture, but also by releasing shear stress associated with the perturbation of the effective poro-elastic stress field and/or by triggering the release of pre-existing tectonic stress. The precise mechanisms of how seismicity is induced remain

an active area of ongoing research, including the causal relationships for its magnitude and spatio-temporal evolution, the role of the network of existing and new fractures, and the relative influence of the natural and perturbed effective stress field (Maxwell 2014).

While induced seismicity from geothermal sites is generally of small magnitude, there is a finite risk of inducing or triggering events that are large enough to be societally relevant, particularly in cases where they are felt or cause damage at the surface. This is particularly important when EGS sites are deliberately located close to urban areas, for example, to act as an efficient local source of heating. Induced seismicity from such geothermal sites unavoidably increases seismic risk, and any induced seismic activity large enough to be felt can result in public alarm in populated regions (Giardini 2009). However, any effective regulatory programme for environmental risk assessment and mitigation or control (e.g. Green *et al.* 2012) requires a better understanding of how seismicity is generated within the reservoir of interest.

There are many detailed case studies of EGS projects associated with induced seismicity, including the Lower Rhine Graben Site in Soultz-sous-Forêt, France (Evans *et al.* 2005) and the Geysers Field

in California, USA (Oppenheimer 1986; Majer *et al.* 2007). These have revealed a series of key factors controlling the induced seismicity, notably the fluid injection rate and the net injection volume (see Section 2); the induced seismicity can be characterised using the total seismic moment released and a related parameter known as the 'seismogenic index' (see Section3). Meanwhile, causative hypotheses including poro-elasticity, the precise mechanisms of fluid–rock interaction (e.g. Shapiro 2015) and the dynamic behaviour of fluid injection (e.g. Verdon *et al.* 2015) have also been developed to explain different aspects of the observations. Computational models incorporating these factors have been developed for the operational forecasting of microseismicity (e.g. Kohl & Megel 2007). However, such models are associated with large uncertainties, and can often significantly underestimate the amount of induced seismicity, primarily due to lack of precise knowledge of the triggering mechanism.

In this paper, we re-examine a rich database of induced microseismicity recorded as part of the UK 'hot dry rock' geothermal experiment at Rosemanowes, Cornwall in the 1980s (Baria *et al.* 1984a,b,c,d, 1983); this was a pioneering project in EGS research and microseismic monitoring of fluid injections. Since the 1980s, our understanding of induced seismicity has improved significantly and new and more sophisticated analysis techniques are available. These techniques include (1) the variation of induced seismicity due to fluid injection (Dahm *et al.* 2012), (2) the calculation of the 'seismogenic index' that reflects the susceptibility of reservoirs to fluid injection (Shapiro 2015) and (3) the propagation of seismic events in reservoirs during fluid injection and the estimation of hydraulic diffusivity based on this propagation (Parotidis *et al.* 2004; Shapiro 2015). Our main goal is to therefore explore the mechanism of induced or triggered seismicity using these modern analysis techniques, and how this relates to the network of pre-existing and new fractures and faults. In this paper, we first briefly introduce the reservoir location, structure and geological context (Section 2). We then demonstrate an unusual deceleration of induced seismicity rate with respect to ongoing fluid injection, despite a net and significant increase in fluid volume in the subsurface, most likely associated with a larger than expected 'sink' of compliant subsurface porosity and storage (Section 3). We then examine the evolution of the 'seismogenic index' as a function of injection and production of fluid (Section 4). We test two hypotheses for the spatio-temporal evolution of the seismicity, namely isotropic and anisotropic porepressure relaxation (Section 5). Finally in Section 6, we summarize a triggering mechanism consistent with the network of pre-existing fractures in the reservoir. This model involves (a) shear slip along the pre-existing joints as the origin of recorded seismicity, (b) aseismic slip with creep, and (c) activated tensile fractures that do not radiate significant seismic energy. This model is consistent with all of the data and known constraints, and provides an internally consistent explanation for how seismicity is generated by fluid injection and the resulting deformation of the reservoir.

2 SITE LOCATION AND GEOLOGICAL BACKGROUND

The geothermal site is located at Rosemanowes Quarry on the Carnnenellis granite (Baria *et al.* 1984c). Its outcrop lies on the continuous ridge of a pluton that extends from Dartmoor to the Scilly Isles in the southwestern part of the UK (Exley & Stone 1964). Gravity studies show that the granite extends to a depth of at least 10 km below the site (Bott *et al.* 1958). Fig. 1 shows the

location of this geothermal site.

The Carnnenellis granite formed in the Hercynian period, early Permian age. It has been subjected to intrusive and tectonic activity throughout its history, and some background tectonic seismic activity is still detectable (Ghosh 1934). The database analysed here has previously been screened to remove the natural seismicity (Baria *et al.* 1984c).

3 INDUCED SEISMICITY AND FLUID INJECTION

The *in situ* operations involved both fluid injection and extraction during the experiment. Stimulation was done by enhanced fluid flow alone, avoiding hydraulic fracturing using propellant (Baria *et al.* 1984a). Cumulative fluid injection into well RH12 is of volume V_I while cumulative fluid production from well RH11 is of volume V_P (Baria *et al.* 1984c). In this paper, we mainly focus on the net injection volume V_N, that is, the difference between the volume injected V_I and produced V_P:

$$V_N = V_I - V_P. \tag{1}$$

The net injected fluid volume is assumed to be contained within the geothermal reservoir. At this stage, we do not consider the loss of fluid outside reservoir during fluid injection. Fig. 2 shows the temporal evolution of the cumulative volume injected and produced, and the resulting net volume stored in the subsurface.

The net injection rate in a certain time window with length Δt is then

$$i_n(t) = \frac{\sum_{t-\Delta t/2}^{t+\Delta t/2} V_N(t)}{\Delta t}. \tag{2}$$

The fluid injection is used to enhance the permeability of the rock mass and hence the majority of the seismicity occurs in the reservoir volume from which heat will be extracted. With this assumption, it is common to use the evolution of the 'cloud' of hypocentres of the induced seismicity to infer properties of the reservoir and how they evolve with time. At Rosemanowes, the seismicity was monitored using a network of vertical-component-only and 3-component accelerometers cemented in boreholes up to 300 m deep (Baria *et al.* 1984c). Downhole calibration shots and VSP surveys were used for velocity model calibration. A half-space model, with station delay terms, was used throughout the project. This is because the granite body containing the reservoir extended to surface outcrop and all ray paths were through the relatively uniform granite body. The catalogue of seismicity used in this study was obtained from recovering and reprocessing the original 1980s waveform data. The data set considered in this study comprises 5184 events located during Phase 2A of the project; this was the main phase of reservoir creation and development. Seismicity also occurred in later phases of the project, but the operational and *in situ* conditions were much more complex and therefore the data have been excluded from this analysis (Baria *et al.* 1984c,d).

The catalogue also lists the scalar seismic moment M_0 inferred from the low frequency asymptote of the source spectra (Andrews 2013). This allows us to examine the relationship between induced seismicity and the temporal variation of the cumulative seismic moment ΣM_0 in Fig. 3.

As in eq. (2), we define seismic moment rate dM_0/dt as the total seismic moment released in a given time interval of duration Δt:

$$\frac{dM_0}{dt} = \frac{\sum_{t-\Delta t/2}^{t+\Delta t/2} M_0(t)}{\Delta t}. \tag{3}$$
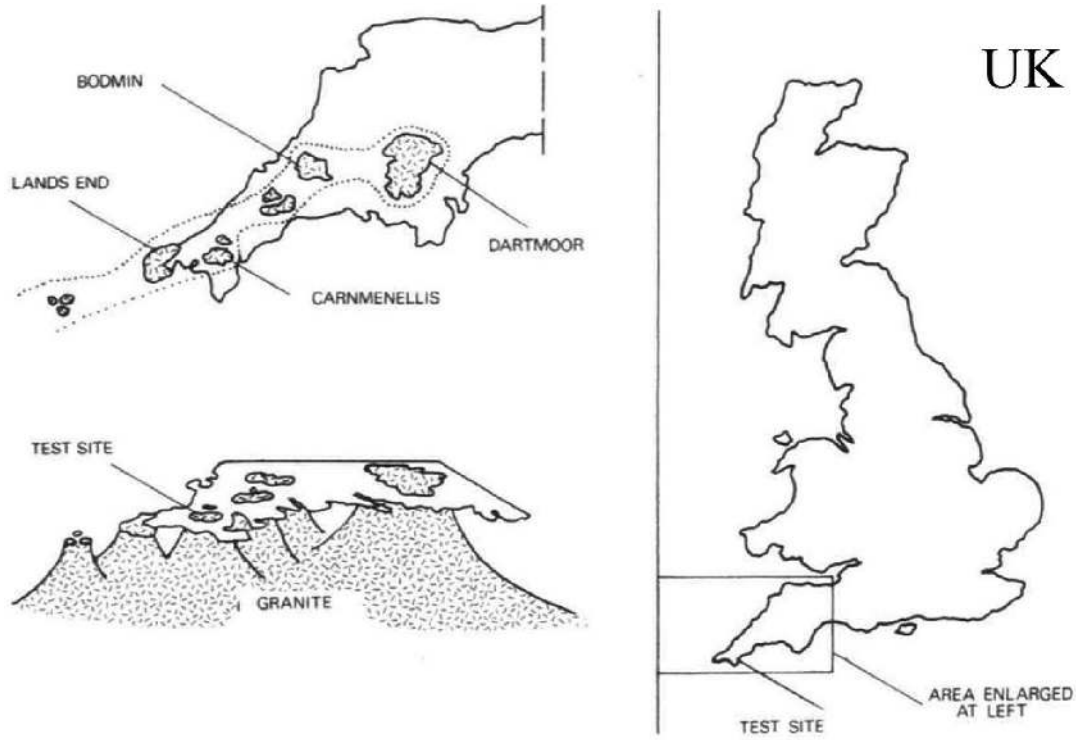
Figure 1. The location of geothermal site at Rosemanowes Quarry, UK and the outline of Cornubian Batholith (Baria *et al.* 1984c).
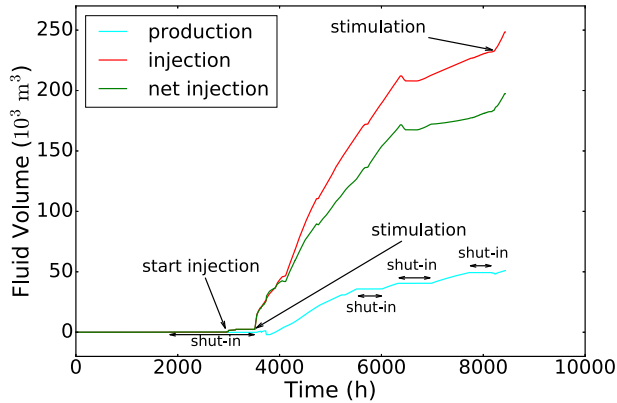

Figure 2. Temporal evolution of cumulative injection, production and net injection volume. The base time of the whole project is at 00:00:00 11 June 1982, reset to zero on the horizontal time axis in units of hours. The vertical axis denotes fluid volume in units of 10^3 m^3. In this graph, a 'shut-in' indicates a period during which production well is closed and hence there is no flow or production. Along the time axis, the first annotated 'stimulation' was carried out to hydraulically fracture the reservoir at a high pressure and injection rate. The second 'stimulation' involves the injection of a viscous fluid for a further development of fracture networks (Baria *et al.* 1984a).

In both eqs (2) and (3), we set the sampling interval Δt to be 30 hr, so that the net injection rate and seismic moment rate refer to the same interval and sampling rate. We choose Δt by trial and error as a pragmatic value that balances the statistical stability of the measure against resolving its temporal evolution.

Previously, Charléty *et al.* (2007) found a strong relationship between seismic moment rate and the net injection rate i_r during fluid stimulation of a geothermal site at Soultz-sous-Forêts, France. Langenbruch *et al.* (2011) conclude that seismicity within this reservoir is directly induced by fluid injection (also see Dahm *et al.* 2012).
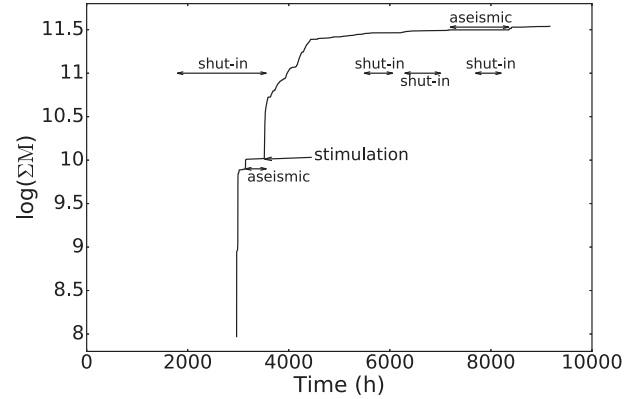

Figure 3. Temporal evolution of cumulative seismic moment. The horizontal axis is time while log in the vertical axis denotes $\log_{10}$. 'Shut-in' denotes a period during which production well is closed while 'stimulation' refers to a period of hydraulic fracture at high injection rates. The label 'aseismic' represents periods when there were no or few seismic events.

Here, we test the hypothesis that there is a relationship between net injection rate i_r and seismic moment rate at Rosemanowes:

$$\frac{dM_0}{dt} = f(i_r). \qquad (4)$$

Then, by combining eqs (2)–(4), we obtain

$$\frac{\sum_{t-\Delta t/2}^{t+\Delta t/2} M_0(t)}{\Delta t} = f\left(\frac{\sum_{t-\Delta t/2}^{t+\Delta t/2} V_N(t)}{\Delta t}\right), \qquad (5)$$

where Δt in the LHS is equal to that in the RHS of eqs (2) and (3). We further assume f is linear, namely $dM_0/dt \propto i_r$, at least to first
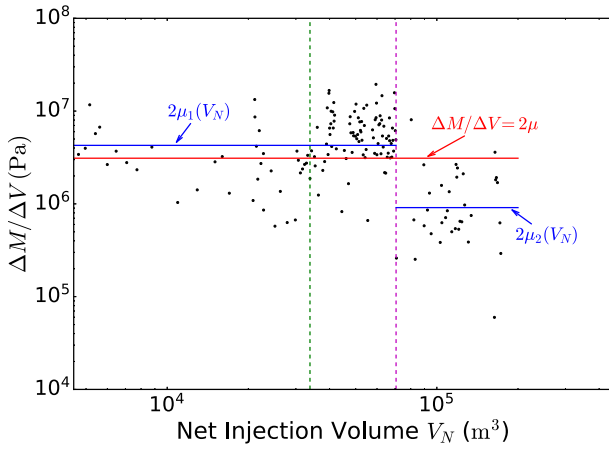
Figure 4. Temporal variation of apparent shear modulus μ_{ap} with respect to the net volume of fluid V_{N} injected in a given time interval. The red line represents eq. (8) ($2\mu_{\text{N}} = 3.1 \times 10^6$ Pa) while the segmented blue line is the best fit to the step function in eq. (11). Here, there are two apparent shear moduli: $2\mu_1(V_{\text{N}}) = 4.3 \times 10^6$ Pa and $2\mu_2(V_{\text{N}}) = 0.85 \times 10^6$ Pa. The magenta dashed line indicates the change point $V_{\text{C}} = 70\,600\,\text{m}^3$ in eq. (11) and the cyan dashed line indicates the change point $V_{\text{C}} = 80\,600\,\text{m}^3$. The green dashed line indicates the switch-on of the production well.

order. Hence, we simplify eq. (5) by removing Δt:

$$\sum_{t-\Delta t/2}^{t+\Delta t/2} M_0(t) = f\left(\sum_{t-\Delta t/2}^{t+\Delta t/2} V_{\text{N}}(t)\right). \qquad (6)$$

We then write $\sum_{t-\Delta t/2}^{t+\Delta t/2} M_0(t)$ and $\sum_{t-\Delta t/2}^{t+\Delta t/2} V_{\text{N}}(t)$ as ΔM_0 and ΔV, respectively, so that

$$\Delta M_0 = f(\Delta V), \qquad (7)$$

where with finite sampling, both ΔM_0 and ΔV are discrete functions rather than continuous ones. For consistency, ΔM_0 and ΔV are calculated at the same sampling points on the time axis.

The two variables in eq. (7), ΔM_0 and ΔV, are independent. The ratio of the two variables defines an apparent shear modulus μ_{ap}:

$$\mu_{\text{ap}} = \frac{\Delta M_0}{2\Delta V}. \qquad (8)$$

We can then define a dimensionless strain partition factor η by the ratio of μ_{ap} and μ where the latter is the actual shear modulus, representing an upper bound to μ_{ap} for seismicity that is induced:

$$\eta = \frac{\mu_{\text{ap}}}{\mu} = \frac{\Delta M_0}{2\mu\Delta V}. \qquad (9)$$

The strain partition factor η is the fraction of the seismically released moment to the total moment expected by injecting a volume of fluid ΔV into the host rock. Typically, η is much less than one (McGarr 2014). If all of the strain is released seismically, then we have $\eta = 1$, also by definition an upper bound for the term 'induced' seismicity. If the tectonic strain is also released or triggered, then this limit does not hold and $\eta > 1$ is possible (Atkinson *et al.* 2016), though this is unusual.

The temporal variation of the apparent shear modulus is plotted in Fig. 4. The data show a significant scatter around the best-fit lines, due to a combination of natural variability and the finite temporal sampling involved in eq. (5).

In Fig. 4, we test two potential models for the evolution of induced seismicity. Model 1 assumes the apparent shear modulus is a constant (red line), and Model 2 involves a step change of the form

of eq. (11) (segmented blue line). Model 1 is denoted by f_1 while Model 2 is denoted by f_2:

$$f_1(V_{\text{N}}) = 2\mu_{\text{ap}} = 3.1 \times 10^6 \ (Pa), \qquad (10)$$

$$f_2(V_{\text{N}}) = 2\mu_{\text{ap}}(V_{\text{N}}) = \begin{cases} 4.3 \times 10^6 \ (Pa) & \text{if } V_{\text{N}} < 70600 \ m^3 \\ 0.85 \times 10^6 \ (Pa) & \text{if } V_{\text{N}} < 70600 \ m^3 \end{cases} \qquad (11)$$

For model 1, the geometric mean of $(\Delta M/\Delta V)_i$ is 3.1×10^6 Pa. For model 2, the first geometric mean is 4.3×10^6 Pa and the second (after the step) is 0.85×10^6 Pa. The optimal value of the change point $V_{\text{C}} = 70\,600\,\text{m}^3$ was determined using a Bayesian Information Criterion (Main *et al.* 1999), as follows.

For Model 1, we first calculate its maximum log likelihood:

$$L(Y) = -\frac{n}{2} \ln(R_1^2). \qquad (12)$$

In eq. (12), $Y(y_i : y_1, y_2, ..., y_K)$ is the set of logged data points $\log(\Delta M_0/\Delta V)_i$ in Fig. 4 and R^2 is the residual sum of squares:

$$R_1^2 = \sum_{i=0}^{K} (y_i - f_1(y_i))^2. \qquad (13)$$

We transform the y-axis to log coordinates because the residuals on Fig. 4 appear log-normal. By fitting to logarithmic values we obtain a geometric mean. This avoids any bias that might be introduced by assuming the residuals were normally distributed around the arithmetic mean. The Bayesian Information Criterion for Model 1 (constant geometric mean) is given by

$$\text{BIC}_{\text{con}} = L(Y) - \frac{1}{2}p\ln\left(\frac{n}{2\pi}\right), \qquad (14)$$

where p is the number of unknown parameters; hence $p = 1$.

We then calculate the maximum log likelihood as in eqs (12) and (13) but with Model 2 using f_2. This involves three parameters, the two geometric means and the optimal change point V_{C}, whence

$$\text{BIC}_{\text{step}}(V_{\text{C}}) = L(Y, V_{\text{C}}) - \frac{1}{2}p\ln\left(\frac{n}{2\pi}\right), \qquad (15)$$

where $p = 3$. Prior to calculating the two geometric means, we first maximize $\text{BIC}_{\text{step}}(V_{\text{C}})$ in eq. (15) as a function of V_{C}. The result is $V_C = 70\,600\,\text{m}^3$, where $\text{BIC}_{\text{step}}(V_{\text{C}}) = \text{BIC}_{\text{max}}$. By comparing BIC_{con} and BIC_{max}, we find

$$\Delta\text{BIC} = \text{BIC}_{\text{max}} - \text{BIC}_{\text{con}} = -249.6 - (-290.9) = 41.3. \qquad (16)$$

BIC_{con} for Model 1 is much smaller than that for Model 2, implying a relative likelihood of $\exp(20.6)$, providing compelling evidence that Model 2 is preferred, and that the step is real.

The step function reflects a sudden and large decrease in the apparent shear modulus at a net injection volume of $70\,600\,\text{m}^3$, with an associated reduction in mean strain partition factor at this change point of a factor of 4 or so. This occurs in Figs 2 and 3 after the third shut-in, and prior to the onset of a relatively aseismic phase of deformation. Given a typical shear modulus of μ of around 3.1×10^{10} Pa for common granites, the absolute value of the inferred strain partition factor is around 10^{-4} at this geothermal site. Such a low value is not uncommon (McGarr 1976), but the implied deceleration in seismic moment release rate with respect to net injected volume is uncommon.

In summary, there appears to be a sudden deceleration of induced seismicity with respect to net injected fluid volume at this geothermal site, and the induced seismicity itself is limited to some 0.01 per cent of the available total strain induced by the fluid injection. This large component of aseismic deformation is consistent with

the deformation being dominated by recoverable strain through the reservoir's relatively compliant poro-elastic response to elevated fluid pressure and/or irrecoverable strain by aseismic displacement, in tension and/or shear.

4 STATISTICAL PROPERTIES

So far we have used the seismic moment listed in the catalogue because of its relationship to the total seismic strain. It can also be related to the more conventional magnitude scale through the calibration introduced by Kanamori (1977) and Hanks & Kanamori (1979). The 'seismic moment magnitude' scale M_w is defined by a logarithmic relationship to the seismic moment M_0 of the form

$$M_w = \frac{2}{3}(\log_{10} M_0 - 9.1), \tag{17}$$

where the seismic moment is in units of N·m. Elsewhere in this paper, we use log to denote the common logarithm $\log_{10}$.

Small earthquakes occur much more frequently than large earthquakes (Greenhough & Main 2008), both for natural and induced seismicity. The frequency–magnitude relationship nearly always takes the form of the Gutenberg–Richter (GR) law (Gutenberg & Richter 1954):

$$\log N_{\geq M_w} = a - bM_w. \tag{18}$$

Here, M_w is the seismic moment magnitude and $N_{\geq M_w}$ is the number or frequency of events with seismic moment magnitude greater than or equal to M_w; a and b are empirical constants. It is well known that applying standard least-squares regression models to cumulative frequency data provides a biased answer due to inherent correlations between data points. In the case of incremental frequencies, a least-squares regression would fail if the sampling or counting errors in N are non-Gaussian and/or vary systematically with magnitude (Greenhough & Main 2008), both of which are relevant for the relatively small numbers involved in many of the data points here. Accordingly, we fit the line using the Maximum Likelihood Method (e.g. Reiter 1991; Bozorgnia & Bertero 2004; Lombardi *et al.* 2005; Kossobokov 2006), originally introduced by Aki (1965). This provides an analytical solution to the inverse problem for determining the exponent b, of the form

$$b = \frac{\log_{10}(e)}{\overline{M}_w - M_c}. \tag{19}$$

Here, e is the base of the natural logarithm and $\overline{M}_w$ is the average seismic moment magnitude for events at or above the cut-off magnitude M_c determined by the threshold of complete detection at a sufficiently high signal-to-noise ratio. Since magnitude is usually reported only to one decimal place (as plotted on Fig. 5), the effective threshold is one-half of a bin width less than the mean value M_c of the relevant bin. Here, we determine M_c using the point where the data points at low magnitude deviate significantly from the GR law (Cao & Gao 2002), whence $M_c = -1.0$. This relatively low threshold is enabled through the use of the downhole sensors mentioned in Section 3 and the low attenuation of the granite body containing the seismicity. The even smaller events recorded could be due to events occurring close to the sensors, or having an unusually high-stress-drop source with unusually short duration and high amplitude, in either case representing a biased sample below M_c. We also solve for the best estimate of the variable a. For consistency, we also use the Maximum Likelihood Method, where the trial a' provides the best estimate of the underlying a when the likelihood
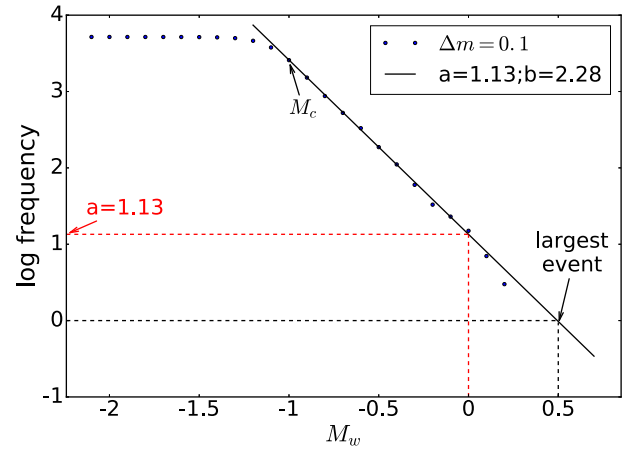

Figure 5. Cumulative frequency–magnitude plot for the induced seismicity at Rosemanowes. The vertical axis is on the common log scale, representing the number of events whose magnitudes are greater than or equal to M_w. The maximum likelihood solution for the GR parameters (straight line) is $a = 1.13$ and $b = 2.28$. The solid black data points are plotted using a bin value $\Delta M_w = 0.1$. The best-fit line indicates $M_c = -1.0$. The largest possible event $M_w = 0.5$ is shown by black dashed lines while red dashed lines indicate that a is the actual value of $\log N$ at $M_w = 0$.

L is a maximum:

$$\left. \frac{\partial L}{\partial a'} \right|_{a'=a} = 0. \tag{20}$$

Using this method, we obtain $a = 1.13 \pm 0.18$ (see Bender 1983) and $b = 2.28 \pm 0.21$ with uncertainties quoted at 95 per cent confidence (Aki 1965; Shi & Bolt 1982; Marzocchi & Sandri 2003; Roberts *et al.* 2015). The slope b is visually a good fit to the data and a is close to the actual value of $\log N$ at $M_w = 0$ (see red dashed lines in Fig. 5). The inferred value of b is relatively high compared to $b = 1$ for global tectonic earthquakes. This in turn is consistent with a relatively low effective stress intensity (a measure of the degree of stress concentration on the largest fault or fracture), since b-value is higher for lower stress intensities in laboratory tests (Sammonds *et al.* 1992). Low stress intensity can arise when (a) the effective stress is relatively low, and/or (b) the stress is not concentrated on a highly localized zone or macrocrack. The former is consistent with the large reservoir storage volume, and the latter with the cloud of epicentres, both of which are examined in more detail in Section 5.

The strain partition factor is not the only metric used to quantify the degree of seismic activation with respect to time or between different injection or depletion sites. Shapiro (2015) defines a seismogenic index Σ to represent the susceptibility of reservoirs to events induced or triggered by fluid injection and extraction, and applies it to a wide range of hydraulic fracturing reservoirs for shale gas and oil production, as well as geothermal reservoirs, to examine its variability in time and space. The seismogenic index is defined by

$$\Sigma \equiv \alpha + \log \frac{C_N}{C_{max}S}, \tag{21}$$

where α denotes the log of event probability with magnitudes larger than zero, S is the storage coefficient, C_{max} is the maximum critical pressure of pre-existing cracks in the reservoir and C_N is the bulk concentration of the pre-existing cracks in the reservoir. The α-value in eq. (21) is connected to eq. (18) using $\alpha = a - \log(N_c)$ where N_c is the number of seismic events with magnitude larger than the cut-off magnitude M_c. Such fractures are likely to be much more
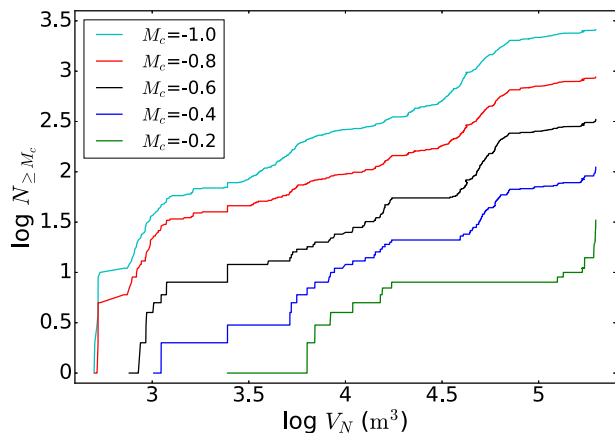
Figure 6. Relationship between $\log N_{\geq M_c}$ and $\log V_N$ as a function of varying (threshold) seismic moment magnitude M_c.

compliant than the otherwise relatively stiff crystalline host rock, and so exert a disproportionate influence on the storage volume in an otherwise tight medium. In summary, the seismogenic index Σ depends only on parameters that reflect the pre-existing effective stress state, the degree of initial damage (natural fracturing and faulting) and the total volume injected up to a given point. It has also been used to assess seismic hazard (Shapiro *et al.* 2010).

In the case of monotonic injection (Shapiro 2015), the seismogenic index can be approximately given by

$$\Sigma = \log N_{\geq M_c} - \log V_N(t) + bM_c. \qquad (22)$$

$N_{\geq M_c}$ is the number of events with magnitudes greater than or equal to the threshold M_c as before, while b is also the value obtained from the GR law (Dinske & Shapiro 2012). Defined in this way, the seismogenic index does not depend strongly on the precise value of M_c, as long as the data are complete above the threshold.

We now apply this parameter to assess the seismic susceptibility of the reservoir to perturbations in effective stress associated with net fluid injection volume V_N. Fig. 6 shows the relationship between $\log N_{\geq M_c}$ and $\log V_N$ with respect to the choice of M_c. All of these thresholds are at or above the minimum threshold of M_c determined by the departure from the GR law in eq. (18). This graph shows that when $M_c \leq -0.4$, the lines are generally parallel to each other with a slope approximately equal to 1, as expected from eqs (18), (21) and (22). For the case $M_c = -0.8$, we obtain a seismogenic index of $\Sigma = -4.2$.

The temporal evolution of seismogenic index Σ can be inferred by combining the results of Figs 2 and 6, transforming from the net injection volume V_N to the equivalent time, as in Fig. 7. The results show a strongly variable convergence to a stable value of $\Sigma = -4.2$. Given the large uncertainties associated with the small numbers of events in the early part of the catalogue, this is not inconsistent with a temporally constant underlying seismogenic index. The value of the seismogenic index is relatively low compared to other geothermal reservoirs worldwide (Shapiro 2015), typically $\Sigma \geq -3.0$, though more consistent with the lower values commonly reported for unconventional hydrocarbon reservoirs. The relatively low value of seismogenic index Σ compared to other geothermal reservoirs is consistent with the low seismic strain partition factor discussed earlier, and highlights the fact that the seismic susceptibility to net injected volume, just like the effective stress intensity inferred from the b-value in the GR law, is anomalously low at Rosemanowes. We explore possible underlying mechanisms for these inferences in the next section.
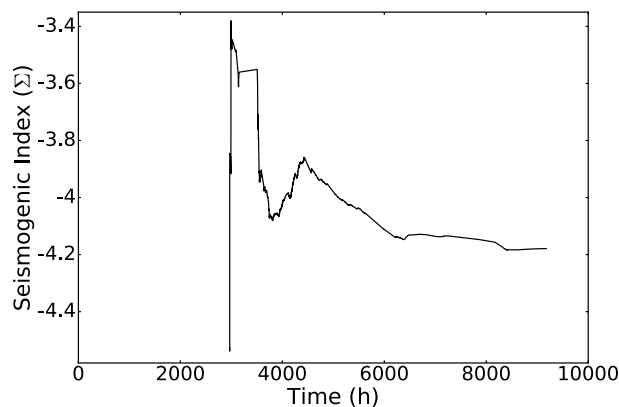

Figure 7. Temporal variation of the seismogenic index in the geothermal reservoir at Rosemanowes.

5 MODELS FOR FLUID FLOW

We now consider two competing hydraulic models for the evolution of the cloud of microseismicity induced by fluid injection into the subsurface. Both are based on the classical triggering mechanism of Nur & Booker (1972) and Fletcher & Sykes (1977) where local failure is triggered passively by a local decrease in the effective normal stress associated with increased pore pressure in the reservoir, as fluid flows away from the borehole to relax the high pore pressure there. This effective stress change is expressed as a modification to the Coulomb stress. If the Coulomb stress change is positive, then this moves the system closer to the envelope of frictional failure in the case of pre-existing joints, fractures and faults (Goodman 1976). This can occur by decreasing the effective normal stress ('unclamping') or increasing the shear stress, or both.

For a medium with both heterogeneous and anisotropic hydraulic diffusivity, this takes the most general form:

$$\frac{\partial p_p}{\partial t} = \frac{\partial}{\partial x_i}\left(D_{ij}\frac{\partial p_p}{\partial x_j}\right), \qquad (23)$$

where we use the Einstein convention as a notation (Shapiro *et al.* 1999). Here, D_{ij} are elements of the tensor of hydraulic diffusivity, which in the general case varies with position along the flow path, and x_i ($i = 1, 2, 3$) are components of the vector from the injection point to a given location in the reservoir. Here, the injection point is defined by the position of the bottom of injection well RH12. The term p_p is the pore-pressure perturbation with respect to the *in situ* pore pressure prior to fluid injection, and t is the time after the start of fluid injection. The diffusivity tensor is related to the permeability tensor by

$$D_{ij} = \frac{K_{ij}}{\upsilon S}. \qquad (24)$$

Here, K_{ij} is the tensor of hydraulic permeability, v is the dynamic viscosity of the pore-fluid, and S is the storage coefficient.

To test the hypothesis of pore-pressure relaxation, Shapiro *et al.* (1999) suggest using the spatial-temporal evolution of the 'triggering front', which is an envelope containing the spatial locations of the induced seismic events at a time t, to define the maximum distance for the triggering front in terms of distances from the injection point $r(t)$. Strictly, this implies that events are only induced within the relaxation zone behind the front, but often there is a finite but lower probability of remote triggering beyond the relaxation zone, especially if the pre-existing tectonic stresses are near critical (e.g. Maillot *et al.* 1999). Despite its generality, the theory is often applied assuming a homogeneous, isotropic medium (Shapiro (2015)),
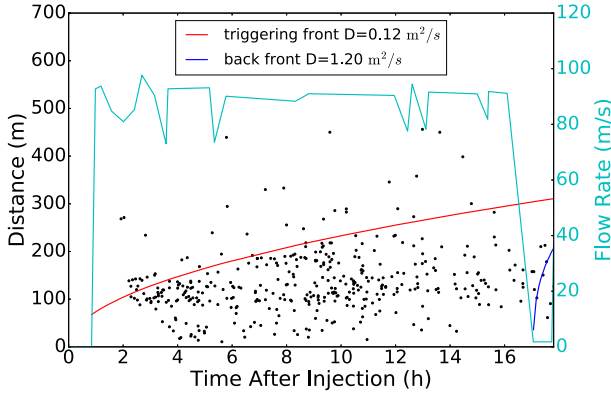
Figure 8. Plot of the distances r_i between the location of the ith event hypocentre and the injection point (dots) and the flow rate as a function of time after the main injection phase (upper curve, right-hand scale). The red curve is the best estimate (by eye) for an envelope function of the flow front of the form $r \propto t^{1/2}$ from eq. (25). The origin time here starts from absolute hour 3513 of the catalogue shown in Fig. 3. The blue curve represents a similar fit for the back front (see eq. 26).

which simplifies the problem to

$$r(t) = \sqrt{4\pi D_{ap} t}, \tag{25}$$

where r is the radius of the spherical triggering front, and the scalar D_{ap} represents the apparent diffusivity in the reservoir. Eq. 25, our first hypothesis, represents Fickian diffusion in a uniform isotropic medium, where $r \propto t^{1/2}$. In general, D_{ap} is affected not only by the intrinsic properties of the host rock but also by feedbacks from fluid injection itself, the presence of fluid channels (including fractures and joints) and the history of fluid injection that is not always injected at a constant rate (see Fig. 2). In the particular case of fluid channelling or anisotropic pore-pressure relaxation, we expect non-Fickian diffusion, where the exponent need not be 1/2 (our hypothesis 2).

If fluid injection terminates at time $t = t_0$, the induced seismicity will continue for a while behind the triggering front for a time $t > t_0$, but will gradually diminish, and eventually cease. The cessation of seismicity defines a propagating 'back front' to the rear of the propagating cloud of events (Parotidis *et al.* 2004). The radius of the back front r_{bf} is given by

$$r_{bf}(t) = \sqrt{2d D_{ap} t \left(\frac{t}{t_0} - 1\right) \ln\left(\frac{t}{t - t_0}\right)}, \tag{26}$$

where d is the spatial dimensionality for pressure diffusion. This is commonly taken to be $d = 2$, that is, assuming planar diffusion (Baria *et al.* 1984a), repeated here for consistency. We test the theory by fitting to a selected time period of 17 hr where the flow rate is relatively high and constant, during the main phase of stimulation after the first shut-in ends, between hours 3513 and 3530 in Fig. 3. Fig. 8 shows both the flow rate and the estimated envelopes for the cloud of distances r for the triggering front and back-front envelopes by using eqs (25) and (26). The best fits were estimated by eye to include around 90 per cent of the data, as is common practice in this method.

There are several points to note in comparing the results of Fig. 8 with the hypothesis of pore-pressure relaxation in a uniform isotropic medium. While the envelope does not contain all of the data points as expected, at early times there are more outside than at later times so the exponent of 1/2 for the curve may not be

optimal. Second, there appears to be a persistent preference for specific values of r, likely associated with persistently active locations after induced events have started (horizontal trends in $r(t)$ amongst the cloud). These could indicate sites that are near-critically stressed prior to injection, and so particularly susceptible to the triggering of brittle failure. The seismicity behind the inferred activation front tends to diminish with time (the density of points reduces at later times), consistent with a transient response to the stimulation. The back front is much harder to fit, but the seismicity implies a higher diffusivity; this indicates that the injection front has increased permeability, most likely by opening fluid flow channels elastically for pre-existing joints and fractures or by seismic (and/or aseismic) dilatant tensile fracture and/or shear. Broadly, we can reject the hypothesis that isotropic pore-pressure relaxation can explain the seismicity, though it may be used to provide a first-order estimate of the permeabilities involved.

We now test the *second* model, which is the hypothesis of the rock mass acting as a homogenous, anisotropic medium. This is consistent with a triggering front of the form

$$\frac{x_1^2}{D_{11}} + \frac{x_2^2}{D_{22}} + \frac{x_3^2}{D_{33}} = 4\pi t. \tag{27}$$

The variables here are the same as those in eqs (23) and (24) but x_i and D_{ii} are in the principal coordinate system. The triggering front generally maps out an ellipsoid surface (Shapiro 2015). This involves stretching the scale in the principal coordinate system relative to those of isotropic diffusion by a factor

$$x_{si} = \frac{x_i}{\sqrt{4\pi t_i}}. \tag{28}$$

Figs 10 and 11 give the lengths of three semi-major axes of the ellipsoid reservoir at the end time of Phase 2A. Scaled by the end time $t_i = t_{end}$ in eq. (28), the ratios of the lengths of the semi-major axes of the scaled ellipsoid are then equal to the ratios of the square roots of the principal diffusivities (Shapiro 2015). Hence, we obtain the principal components of the apparent diffusivity tensor in the principal coordinate system

$$D = \begin{pmatrix} 0.01 & 0 & 0 \\ 0 & 0.03 & 0 \\ 0 & 0 & 1.6 \end{pmatrix} m^2/s. \tag{29}$$

In eq. (29), D_{11} is the apparent diffusivity along the minor axis of the ellipsoid that encloses the seismicity in the reservoir, while D_{22} is the diffusivity along the intermediate axis and D_{33} is the diffusivity along the major axis. Sections of the ellipsoid are shown in Figs 10 and 11. The major axis here is vertical (compare absolute values in Figs 10 and 11). These large variations in the principal components indicate a strong anisotropy of hydraulic diffusivity in the Carnnenellis granite.

In addition to the envelope of induced seismicity defined by the triggering front, we also plot the mean value $\bar{r}$ in a time interval $\Delta t = 1$ hr. The slope of the least-squares regression line in Fig. 9 is 0.382 ± 0.017, where the error is quoted at 95 per cent confidence. This confirms non-Fickian diffusion, in turn, consistent with the anisotropic nature of the seismicity cloud in Figs 10 and 11.

6 FRACTURE NETWORKS AND COMPOSITE FOCAL MECHANISM

In the previous section, we tested different hypotheses for the spatio-temporal evolution of the cloud of microseismicity based solely on the distance from the injection point r as a metric. However, this
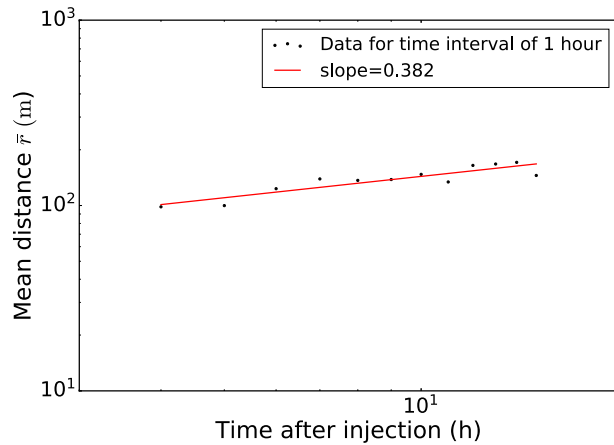
Figure 9. Plot of the mean distances $\bar{r}$, that is, the average distance r_i between the event hypocentre locations and the injection point as in Fig. 8 within a time interval $\Delta t = 1$ hr. The red line is the least-squares regression, one with slope 0.382 ± 0.017, where the error is quoted at 95 per cent confidence. Both horizontal and vertical axes are on log scales.
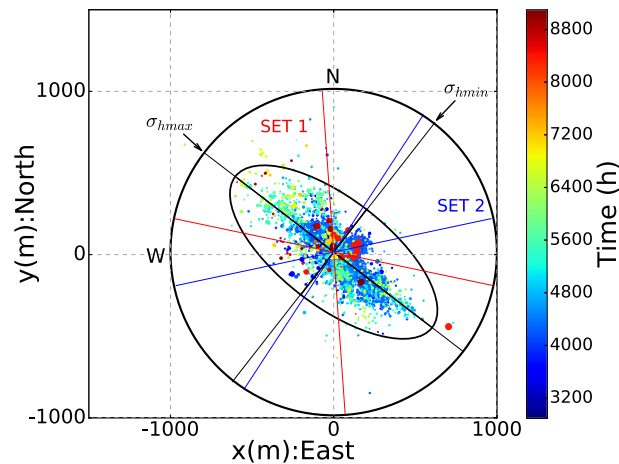

Figure 10. Epicentral map of the induced seismicity (small dots, with occurrence time represented by the colour scale in the key). A best-fit ellipse to the envelope of seismic events is shown, along with its semi-major and semi-minor axes (black solid lines). The injection point is at the centre of the ellipse (yellow square). Overlain on top is a radial diagram showing the horizontal azimuths of the *in situ* stress field and the population of strike orientations for pre-existing joints inferred from the borehole image log (Baria *et al.* 1984c). The labels SET 1 and SET 2 indicate two separate populations of pre-existing subvertical joints: SET 1 from azimuths 282° to 357°, and SET 2 from 033° to 078°. σ_{hmax} with azimuths 308° denotes the maximum horizontal principal stress (70 MPa) while σ_{hmin} with azimuths 038° denotes the minimum horizontal principal stress (30 MPa), both measured in the borehole at a depth of 2000 m.

hides much of the detail of the spatio-temporal distribution in the three different spatial coordinates. In this section, we examine this evolution in detail, along with allied data such as the composite focal mechanism of the events, the ambient stress field and the orientation of the pre-existing joints in the host granite. While cognisant of the challenges involved in determining triggering mechanism (Maxwell 2014), we provide some insights into the mechanisms of induced seismicity at the Rosemanowes test site.

Some 5184 seismic events were recorded during Phase 2A of the project. The spatio-temporal evolution of their locations is shown by the coloured dots in Fig. 10, starting from the near field around the injection point at about 2000 m depth in well RH12 at early times. The microseismic cloud then diffuses outwards with time. An elliptical envelope is drawn with a centre fixed at the injection point; the envelope contains the vast majority of the events—only a few remain outside, mainly to the NW on the map section. This subset could indicate longer range poro-elastic triggering or strong flow channelling in this direction. With this exception, the elliptical triggering front on Fig. 10 outlines the likely extent of the reservoir sampled by fluid flow. The object is an ellipsoid in 3-D, with the longest axis vertical. The axes of the ellipsoid are then vertical (major axis), approximately NW (intermediate), and NE (minor axis), with diffusivities of decreasing magnitude in that order (see Fig. 11). The ellipsoid shape is consistent with an underlying 3-D diffusivity tensor in a relatively uniform but anisotropic medium, with inferred principal axes D_{ii} aligned with the three semi-major axes of the ellipsoid (see eq. 29).

We estimate the total volume of the ellipsoid outlined in Figs 10 and 11, $V_e = 1.41 \times 10^9$ m³. We also know the total net injected volume change V_N. The total dilational strain V_N/V_e is then 1.2×10^{-3}. This strain is significant; for example, it is larger than the typical strain change in a tectonic or natural earthquake of 10^{-4}. This confirms that most of the total strain must be released aseismically, due to (poro-) elastic processes or silent irreversible strain, rather than the seismic strain which accounts for only 0.01 per cent of the total. Such a low seismic strain for such a high total strain is in turn consistent with a large elastic storage volume accessible in an extremely compliant reservoir.

Fig. 10 also shows the orientations of maximum and minimum horizontal stress for reference. These were measured directly in the borehole using hydraulic tests and measurements in deep tin mines. The diagram also shows the range of strikes for the pre-existing subvertical joints (Baria *et al.* 1984a,c). There are two sets of such vertically aligned joints: one aligned with an azimuth between 282° and 357° (set 1 on the diagram) and one in the orthogonal direction (set 2 with an azimuth between 33° and 78°). The orientations of the sets of joints are measured from downhole image log rather than using surface mapping (Baria *et al.* 1984e). The orientation of horizontal major axes of the best-fit ellipse to the seismic cloud is aligned at an azimuth of 307.0° ± 0.8°, where the error is quoted at 95 per cent confidence. This orientation is obtained by least-squares regression applied to the epicentral coordinates for the induced seismic events. The low uncertainty confirms a clear anisotropy of the flow field whose alignment is in turn consistent within error with the orientation of maximum horizontal stress estimated independently from borehole measurements. The directions of maximum horizontal stress and maximum horizontal diffusivity are both subparallel to the central tendency of the pre-existing joint set 1, indicating that the modern-day stress field is slightly rotated from its direction while the joints were formed, or that the host rock itself was strongly anisotropic at the time of joint formation.

The seismicity at Rosemanowes was also analysed for earthquake source mechanism and orientation. The resulting composite focal mechanisms of the induced seismicity, solved from clusters of events, are shown in Fig. 12. The result is a clear double couple from strike-slip to dip-slip faulting. According to the estimation of focal mechanisms in Baria *et al.* (1984c), most events are strike-slip and a few events are normal faulting. The logging report from image logs indicates that most downhole fractures are steeply dipping but a few dip in 50° to 60° in pre-existing joint set 1 (Baria *et al.* 1984e). This implies that most nodal planes (strike-slip) are at an angle of 20° to 40° to σ_{hmax}. The double-couple mechanism is consistent with microseismicity detected in the reservoir being generated by
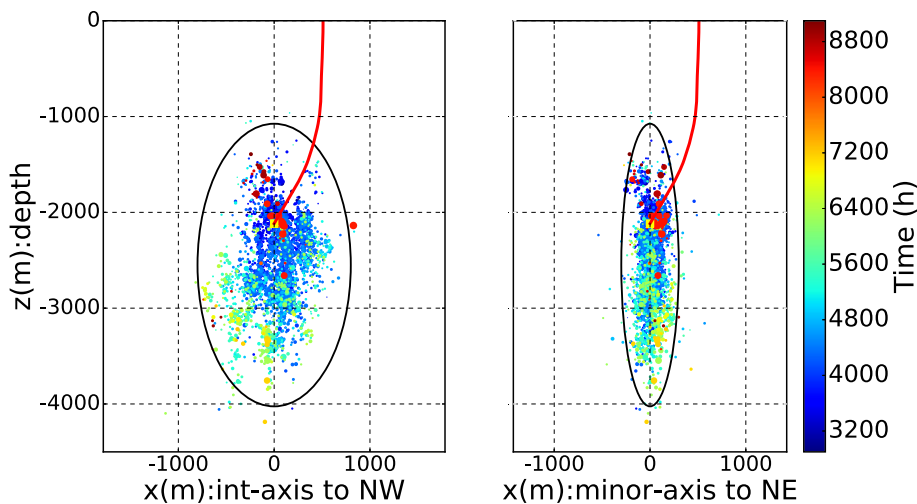
Figure 11. Two cross-sections for depth versus the coordinates of the intermediate and minor axes in Fig. 10. (a) The plane of the plot is on the intermediate axis and major axis. (b) The plane of the plot is on the minor axis and major axis. Note that all axes in these two cross-sections are on same length scale. The red solid line displays the oblique injection well, and the injection point is denoted by the yellow square.
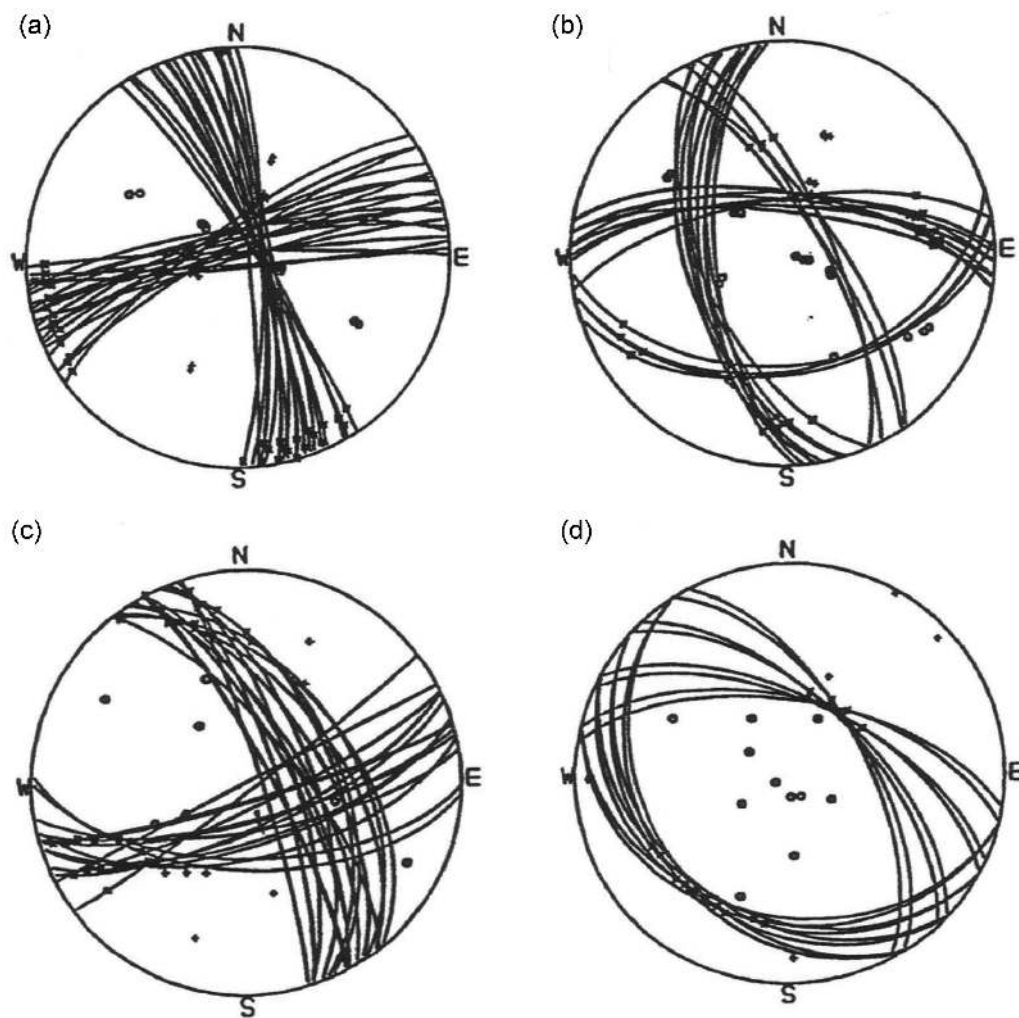

Figure 12. Standard composite solutions derived from data recorded at Rosemanowes (adapted from Baria *et al.* 1984c). Panels (a)–(d) show a range of focal mechanisms from small clusters of events. The frequency of these focal mechanisms decreases in the order of (a) strike-slip, (b, c) oblique and (d) normal faults that are few.

dynamic shear slip, with a vertically aligned intermediate principal stress and null axis, and no seismic radiation from tensile cracks on the pre-existing joint set 2 (see also Baria *et al.* 1984c). There are two nodal planes in Fig. 12(a), one subparallel to joint set 1 (Baria *et al.* 1984c) and the other to be set 2 at an azimuth of about 60°. However, the present-day *in situ* stress field would be likely to apply a low normal stress to set 1 joints and a high normal stress to set 2 joints, so the most likely slip plane is the nodal plane subparallel to joint set 1, that is, oriented at an azimuth of about 320°. Finally, the null axis of the stress field is vertical, implying the maximum horizontal stress is also the maximum principal stress, whereas the maximum diffusivity is aligned in the vertical direction. This indicates that the flow field also requires a strong, pre-existing or created hydraulic structure, in the form of a vertically aligned channel, to crack opening by stress alignment in the horizontal direction.

The strikes of set 1 joints range from an azimuth of 282° to 357°. The orientation of 339° (31° to σ_{hmax}) is optimal for reactivation in shear according to the Coulomb frictional theory, which is consistent with the strike and slip direction of the most frequent composite focal mechanism slip plane (see Fig. 12a). Accordingly, we conclude that the shear slip along the pre-existing joint set is a direct cause of the observed seismicity. The water injection preferentially activates (1) tensile fractures aligned towards the NW and (2) pre-existing shears which in turn open the set 2 joints as illustrated in Fig. 13.

7 DISCUSSION

The re-analysis of the data from the geothermal site at Rosemanowes provides a number of findings, as follows:

(1) The apparent shear modulus and strain partition factor are extremely low at this site. We conclude that the seismicity releases only a small fraction (0.01 per cent) of the total available strain implied by the net fluid injection.

(2) The dimensionless volumetric strain derived from the volume of the seismic cloud and net fluid injection is however high, on the order of 10^{-3}. This is more than the typical requirement to produce significant seismic strain release (typically 10^{-4} in earthquake scaling).

(3) We also identify an unusual step-change deceleration in seismicity and decrease in the strain partition factor with ongoing fluid injection.

(4) The seismogenic index Σ is both anomalously low and decreases systematically with ongoing fluid injection at this geothermal site. We note that a low value of Σ is often found at hydraulic fracturing sites for shale oil and gas production, but it is less common for geothermal sites (Shapiro 2015).

(5) We observe that the evolution of the envelope of triggering distances (i.e. the triggering front) $r(t)$ is not consistent with Fickian diffusion, but is consistent with a model based on anisotropic diffusion in an otherwise homogeneous medium.

(6) An extremely permeable channel appears to exist along the vertical axis of the reservoir, which corresponds to the intermediate principal stress direction.

(7) We conclude that the relationship between subsurface deformations and associated induced seismicity is consistent with much of the independent estimation of the stress field and the pre-existing joint pattern. However, a range of focal mechanisms is observed, mainly strike-slip subparallel to maximum principal stress, apart from some with distinct normal faulting components. The complex and various focal mechanisms involved still raise questions on the true triggering mechanism.

We now discuss these issues further, explore the relationship between hydraulic injection and induced seismicity in the geothermal site at Rosemanowes and suggest a hypothesis for induced seismicity consistent with all of the known constraints.

7.1 A compliant fracture system and fluid storage

The low strain partition factor η implies that only 0.01 per cent of the total deformation is seismic and the rest is aseismic. This further implies that the vast majority of the deformation in the reservoir is either elastic, or inelastic in the form of undetectable hydrofracture events, small shear-slip earthquakes or stable slip by aseismic creep. Furthermore, the inferred volumetric strain at the reservoir scale is an order of magnitude higher than the seismic strain coefficient, implying a significant storage of elastic strain energy within the rock mass.

The decrease of the apparent shear modulus μ_{ap} and the strain partition factor η with ongoing fluid injection also implies that aseismic processes become increasingly important as fluid circulates around the reservoir at pressure. The breakpoint $V_C = 70\,600$ m^3 in Fig. 4 is just after the start of the circulation phase of the project (Baria *et al.* 1984a). This may be connected with the change in operational mode at the start of circulation. Both wells have been highly stimulated and now water is just being circulated between the two wells. The pressures are still high, but the reservoir is no longer expanding, in terms of an increasing seismic cloud volume. The breakpoint may indicate that water injection in the circulation phase pervades the whole reservoir volume and further suppresses seismic activity. Thus, a lower strain partition factor might be expected during the circulation phase. Although this explanation seems plausible, we cannot completely rule out (1) a problem with the old seismic data set that is recovered from a historic waveform format and (2) some data recording gaps occasionally due to instrumentation problems (Baria *et al.* 1984c).

We also note that a highly compliant fracture system would tend to lead to a relatively low pressure environment, which is below the threshold needed for hydraulic fracturing. This is supported by the fact that the operators found it difficult to increase the downhole pressure above the minimum effective stress of 10 to 12 MPa (Baria *et al.* 1984a). The tensile strength of granite is about 10 MPa, so we can exclude shear slip on new hydraulic fractures in the geothermal site at Rosemanowes.

The net volume produced is a small fraction of that injected, implying a significant volume of fluid stored in the subsurface, or lost to the far field. This is also consistent with the relatively compliant system of pore space and tensile cracks inferred in the previous subsection. To explore this further, we transform eq. (22) into

$$\Sigma = \log \frac{N_{\geq M_c}}{V_N(t)} + b M_c. \tag{30}$$

Eq. (30) indicates that for the same frequency–magnitude relationship $N_{\geq M_w}$, more fluid volume is required to produce a relatively lower seismogenic index Σ, assuming M_c and b are constant. A high fluid storage within the subsurface is thus also consistent with the low seismogenic index.

Another implication on the high net fluid storage in the reservoir comes from the compliant fracture system. The key observations are (1) that as injection pressure increases, the production rate increases and (2) that water loss (leak-off) to the far field also increases dramatically (Baria *et al.* 1984a). When the injection pressure decreases, both the production rate and water loss decrease, consistent
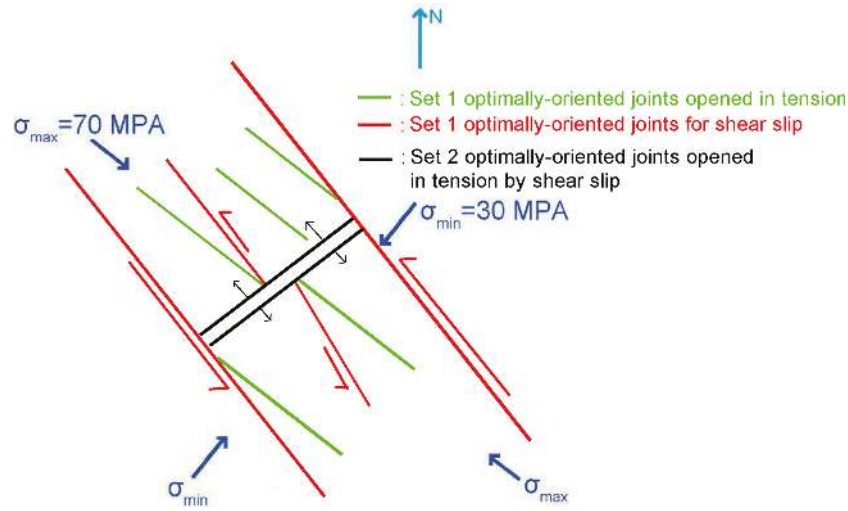
Figure 13. Schematic model for the relationships between the average orientation of the fracture networks in the reservoir and the *in situ* stress field at the injection depth. The red lines show the sense of shear slip; we would expect the slip on the pre-existing set 1 joints in the present-day stress field. σ_{max} is the maximum horizontal principal stress while σ_{min} is the minimum principal stress, with the intermediate principal stress being vertical. The green lines indicate the tensile fractures, aligned with σ_{max}. The black lines represent the average orientation of set 2 joints, as an example. The seismic and aseismic shearing on pre-existing set 1 joints causes pull-apart of pre-existing set 2 joints, which leads to fracture growth and further enhances vertical permeability (Baria *et al.* 1984f).

with an instantaneous elastic response. The vertical fracture growth discussed below is one potential mechanism for high water loss at the geothermal site of Rosemanowes.

7.2 Non-Fickian diffusion and anisotropic permeability

Fick's second law is the standard diffusion equation for an isotropic and uniform diffusion constant in space and time (Crank 1979). Accordingly, we take 'non-Fickian' diffusion to describe a more general case where the diffusion constant depends on position, time or direction of flow. This includes cases where diffusivity varies permanently from place to place due to material heterogeneity, where stress anisotropy leads to permeability anisotropy or where there is feedback between pore pressure and diffusivity locally due to poro-elastic effects. The latter is an example of non-linear diffusion due to the feedback involved (Economides & Nolte 2000; Shapiro & Dinske 2009; Hummel & Shapiro 2012, 2013, 2016). These different mechanisms may result in channelling, flow anisotropy and non-Gaussian breakthrough profiles for a spike input at the source. Non-Fickian diffusion is sometimes called 'anomalous diffusion', though it is actually quite common in subsurface fluid flow problems (Berkowitz & Scher 1997, 1998). A key diagnostic of non-Fickian diffusion is power-law scaling of mean distance travelled versus time, with an exponent different from the standard Fickian exponent of 1/2 (Glasbey 1995).

The non-Fickian diffusion of the envelope enclosing the seismicity is consistent with a model for strong flow channelling along optimally oriented joints; this consistency is implied by the poor fit of the envelope with exponent 1/2 to the data on Fig. 8. It is also consistent with the inferred compliant nature of the aligned fracture systems observed in the borehole image logs, and the anisotropic fluid flow field in the reservoir inferred from the shape of the seismicity cloud on Fig. 11. The focal mechanism for the small seismic component of the deformation implies sinistral strike-slip shear, but the overall behaviour of the pressurization indicates deformation is dominated by aseismic crack opening, consistent with the observation $r \propto t^{0.382}$. We therefore conclude that (1) fluid flow is

non-Fickian in the reservoir and (2) the most likely mechanism is flow channelling by anisotropic pore-pressure relaxation.

A significant feature of the flow channelling is that an extremely permeable channel appears to exist in the vertical direction of the reservoir. Using eq. (29), the vertical permeability is found to be almost two orders higher than that in the horizontal directions, one along the major axis of the reservoir ellipse and the other along the minor axis in Fig. 10. This behaviour can be explained by the following model.

There are a number of issues to take into account in providing an holistic interpretation for the observations above. To summarize, we require a mechanism that explains (1) seismic slip for the recorded induced seismicity, (2) aseismic slip to explain the low strain partition factor, (3) the presence of activated existing tensile fractures consistent both with the low seismogenic index Σ and the non-Fickian diffusion of $r(t)$, (4) the high fluid storage/loss in the reservoir and (5) that an extremely permeable channel exists in the vertical direction of the reservoir.

We follow a conceptual mechanism proposed in Harper & Last (1989) and Baria *et al.* (1984f) consistent with these constraints in Fig. 13. Tensile fracture openings by seismic and aseismic shearing on pre-existing set 1 joints (NW/SE striking) are critical in creating vertical fluid channels and permeability anisotropy in the reservoir, as well as controlling the diffusion of induced seismicity away from the injection point. The shear slip on the subvertical set 1 joints can pull the set 2 (NE/SW striking) joints apart, promoting strong vertical channelling of flow. Following the conceptual mechanism of vertical fracture growth proposed in Harper & Last (1989), a strong permeability in the vertical direction and high fluid storage/water loss appears highly probable in a well-connected fracture system.

On the horizontal plane, the orientation of the best-fitting major axis of the elliptical envelope around the cloud of induced seismicity coincides with the maximum principal stress direction. The orientation of tensile fractures is also (1) subparallel to the minimum principal stress direction and (2) consistent with the opening in the direction of set 2 joints. However, an injection pressure well below the tensile strength of granite (about 10 MPa) excludes the

possibility of hydraulically created tensile fractures along maximum principal stress direction (Maxwell 2014, and references therein). The double-couple nature of the composite focal mechanism also implies that any hydraulic tensile fractures along set 2 joints, while likely to be dynamically induced near the injection point, remain below the threshold of detection by the seismic network.

7.3 Dip-slip events

In Fig. 12, we also see some focal mechanisms that are dip-slip rather than strike-slip in most cases. From downhole imaging (Baria *et al.* 1984e), most of the natural fractures are subvertical (e.g. pre-existing joint set 1 and 2), but there is a much smaller proportion with a shallower slip and a normal faulting mechanism. Combined with Fig. 10, we can estimate the minimum pressure of shear failure (Coulomb type) is preferential for vertical fractures striking at 20° to the maximum horizontal stress. However, the pressure required for shearing dipping fracture striking close to σ_{hmax} is really not much higher. Thus, normal faulting focal mechanisms exist because the dipping (set 1) fractures are also close to optimally oriented direction for reactivation in shear.

We therefore conclude the most likely explanation for the overall behaviour of the seismicity is seismic slip, and elastic tensile opening, on optimally oriented pre-existing joint set 1 fractures, coupled with aseismic tensile opening on joint set 2 fractures.

8 CONCLUSION AND PROSPECT

The seismicity induced by the Rosemanowes hot dry rock experiment released only a small fraction (0.01 per cent) of the total available strain by net fluid injection. The dimensionless volumetric strain is relatively high, on the order of 10^{-3}. This implies a very low absolute seismic strain of 10^{-7}, and a correspondingly low seismogenic index. The dimensionless volumetric strain is more than enough to produce significant seismic strain release (typically 10^{-4} in earthquake scaling) within the affected volume (Kanamori 1977). Laboratory measurement shows that a common strain for the onset of damage generating acoustic emission in rocks is on the order of 10^{-5} (Mavko *et al.* 2003). The very low absolute seismic strain at Rosemanowes is consistent with a dominantly elastic response at the reservoir scale, with some aseismic irreversible tensile fracture and seismic slip and a very small proportion of seismic slip.

The large volume of fluid left in the subsurface implies a high degree of storage, and some far-field fluid loss, in a relatively compliant set of fractures with a significant dilatant (tensile opening) component. Unusually, the strain partition factor reduces with ongoing injection, implying that a decelerating rather than a near-critical (accelerating) response to the stress perturbation associated with fluid injection. The diffusion envelope for the distance between the earthquake foci and the injection point is inconsistent with fluid flow in a uniform isotropic medium, but it is consistent with a model for fluid flow channelled by flow along pre-existing microfractures aligned parallel to the direction of maximum principal stress in an otherwise uniform medium. The locations of the earthquake foci in 3-D reveal anisotropic diffusion aligned with principal stresses of the *in situ* stress field. The major difference is that the maximum inferred permeability is in the vertical direction, whereas the maximum principal stress is horizontal, implying a pre-existing compliant or permeable structure with the tensile fracture opening during the injection process must be primarily responsible for the vertical channelling.

The composite focal mechanism is consistent with the dynamic reactivation of optimally oriented natural joints in shear mode. However, the injection pressure is well below the tensile strength of granite in the reservoir and therefore excludes any significant dynamic radiation from hydraulic fracturing. Hydraulic fracture (pull-apart) along pre-existing set 2 joints is likely to be dynamic but below the detection threshold for seismicity, whereas aseismic creep by hydraulic unclamping (reducing the effective normal stress by increasing the pore pressure) is the most likely mechanism for reactivation of the optimally oriented set 1 joints, in turn promoted by fluid flow between the subparallel joint sets along stress-aligned tensile cracks.

The composite focal mechanism for seismic events in the main phase of injection is mostly consistent with dynamic slip on preferential pre-existing joint set 1, pulling pre-existing joint set 2 apart to largely enhance vertical permeability.

To our knowledge, this is the first time such a unified model has been proposed for the geothermal site of Rosemanowes, respecting all of the known constraints. It provides a scenario to consider for risk assessment of projects involving geothermal energy extraction from jointed crystalline hot rocks, in Cornwall and elsewhere.

There are still unknowns at the geothermal site of Rosemanowes. In particular, we do not have a strong conclusion on a change of the strain partition coefficient after the start of circulation phase. The hypothesis that pervasive fluid can suppress seismicity in the reservoir needs to be investigated further with several possible problems in the historical data.

REFERENCES

Aki, K., 1965. Maximum likelihood estimation of b in the formula log N = a-bM and its confidence limits, *Bull. seism. Soc. Am.,* **43,** 237–239.

Andrews, D.J., 2013. *Objective Determination of Source Parameters and Similarity of Earthquakes of Different Size,* pp. 259–267, American Geophysical Union.

Atkinson, G.M. *et al.*, 2016. Hydraulic fracturing and seismicity in the Western Canada sedimentary basin, *Seismol. Res. Lett.,* **87**(3), 631–647.

Baria, R., Hearn, K., Lanyon, G. & Batchelor, A., 1983. Camborne School of Mines geothermal energy project, in-situ stress, Tech. rep., Camborne School of Mines.

Baria, R., Hearn, K., Lanyon, G. & Batchelor, A., 1984a. Camborne School of Mines geothermal energy project, hydraulic results, Tech. rep., Camborne School of Mines.

Baria, R., Hearn, K., Lanyon, G. & Batchelor, A., 1984b. Camborne School of Mines geothermal energy project, jointing, Tech. rep., Camborne School of Mines.

Baria, R., Hearn, K., Lanyon, G. & Batchelor, A., 1984c. Camborne School of Mines geothermal energy project, microseismic results, Tech. rep., Camborne School of Mines.

Baria, R., Hearn, K., Lanyon, G. & Batchelor, A., 1984d. Camborne School of Mines geothermal energy project, seismic velocity structure, Tech. rep., Camborne School of Mines.

Baria, R., Hearn, K., Lanyon, G. & Batchelor, A., 1984e. Camborne School of Mines geothermal energy project, logging results, Tech. rep., Camborne School of Mines.

Baria, R., Hearn, K., Lanyon, G. & Batchelor, A., 1984f. Camborne School of Mines geothermal energy project, mechanical and hydraulic modeling, Tech. rep., Camborne School of Mines.

Bender, B., 1983. Maximum likelihood estimation of *b*-values for magnitude grouped data, *Bull. seism. Soc. Am.,* **73**(3), 831–851.

Berkowitz, B. & Scher, H., 1997. Anomalous transport in random fracture networks, *Phys. Rev. Lett.,* **79**, 4038–4041.

Berkowitz, B. & Scher, H., 1998. Theory of anomalous chemical transport in random fracture networks, *Phys. Rev. E,* **57**, 5858–5869.

Bott, M.H.P., Day, A.A. & Masson-Smith, D., 1958. The geological interpretation of gravity and magnetic surveys in Devon and Cornwall, *Phil. Trans. R. Soc.,* **251**(992), 161–191.

Bozorgnia, Y. & Bertero, V., 2004. *Earthquake Engineering: From Engineering Seismology to Performance-Based Engineering,* CRC Press.

Cao, A. & Gao, S.S., 2002. Temporal variation of seismic *b*-values beneath northeastern Japan island arc, *Geophys. Res. Lett.,* **29**(9), 43–48.

Charléty, J., Cuenot, N., Dorbath, L., Dorbath, C., Haessler, H. & Frogneux, M., 2007. Large earthquakes during hydraulic stimulations at the geothermal site of Soultz-sous-Forêts, *Int. J. Rock. Mech. Min. Sci.,* **44**(8), 1091–1105.

Crank, J., 1979. *The Mathematics of Diffusion,* Oxford science publications, Clarendon Press.

Dahm, T. *et al.*, 2012. Recommendation for the discrimination of human-related and natural seismicity, *J. of Seismology,* **17**(1), 197–202.

Dinske, C. & Shapiro, S.A., 2012. Seismotectonic state of reservoirs inferred from magnitude distributions of fluid-induced seismicity, *J. Seismol.,* **17**(1), 13–25.

Economides, M. & Nolte, K., 2000. *Reservoir Stimulation,* Wiley.

Ellsworth, W.L., 2013. Injection-induced earthquakes, *Science,* **341**(6142), 1225942, doi:10.1126/science.1225942.

Evans, K.F. *et al.*, 2005. Microseismicity and permeability enhancement of hydrogeologic structures during massive fluid injections into granite at 3 km depth at the Soultz HDR site, *Geophys. J. Int.,* **160**(1), 388–412.

Exley, C. & Stone, M., 1964. *The granitic rocks of South-West England,* 180th anniversary of the Royal Geological Society of Cornwall.

Fletcher, J.B. & Sykes, L.R., 1977. Earthquakes related to hydraulic mining and natural seismic activity in Western New York State, *J. geophys. Res.,* **82**(26), 3767–3780.

Ghosh, P.K., 1934. The carnmenellis granite: its petrology, metamorphism and tectonics, *Q. J. Geol. Soc.,* **90**, 240–276.

Giardini, D., 2009. Geothermal quake risks must be faced, *Nature,* **462**(7275), 848–849.

Glasbey, C.A., 1995. Non-Fickian diffusion, *Eur. J. Soil Sci.,* **46**(1), 159–159.

Goodman, R.E., 1976. *Methods of Geological Engineering in Discontinuous Rocks,* West Pub. Co St. Paul.

Green, C., Styles, P. & Baptie, B.J., 2012. *Shale gas fracturing review & recommendations for induced seismic mitigation, Tech. rep.,* DECC.

Greenhough, J. & Main, I.G., 2008. A Poisson model for earthquake frequency uncertainties in seismic hazard analysis, *Geophys. Res. Lett.,* **35**(19), 8–11.

Gutenberg, B. & Richter, C., 1954. *Seismicity of the Earth and Associated Phenomena,* 2nd edn, Princeton University Press.

Hanks, T.C. & Kanamori, H., 1979. A moment magnitude scale, *J. geophys. Res. Solid Earth,* **84**(B5), 2348–2350.

Harper, T.R. & Last, N.C., 1989. Interpretation by numerical modelling of changes of fracture system hydraulic conductivity induced by fluid injection, *Geotechnique,* **39**(1), 1–11.

Hummel, N. & Shapiro, S.A., 2012. Microseismic estimates of hydraulic diffusivity in case of non-linear fluid-rock interaction, *Geophys. J. Int.,* **188**(3), 1441–1453.

Hummel, N. & Shapiro, S.A., 2013. Nonlinear diffusion-based interpretation of induced microseismicity: a Barnett Shale hydraulic fracturing case study, *Geophysics,* **78**(5), B211, doi:10.1190/geo2012-0242.1.

Hummel, N. & Shapiro, S.A., 2016. Back front of seismicity induced by non-linear pore pressure diffusion, *Geophys. Prospect.,* **64**(1), 170–191.

Kanamori, H., 1977. The energy release in great earthquakes, *J. geophys. Res.,* **82**(20), 2981–2987.

Kohl, T. & Megel, T., 2007. Predictive modeling of reservoir response to hydraulic stimulations at the European EGS site Soultz-sous-Foréts, *Int. J. Rock Mech. Min. Sci.,* **44**(8), 1118–1131.

Kossobokov, V.G., 2006. Testing earthquake prediction methods: the West Pacific short-term forecast of earthquakes with magnitude MwHRV ≥ 5.8, *Tectonophysics,* **413**(1-2), 25–31.

Langenbruch, C., Dinske, C. & Shapiro, S.A., 2011. Inter event times of fluid induced earthquakes suggest their Poisson nature, *Geophys. Res. Lett.,* **38**(21), 1–6.

Lombardi, A.M., Akinci, A., Malagnini, L. & Mueller, C.S., 2005. Uncertainty analysis for seismic hazard in Northern and Central Italy, *Ann. Geophys.,* **48**(6), 853–865.

Maillot, B., Nielsen, S. & Main, I., 1999. Numerical simulation of seismicity due to fluid injection in a brittle poroelastic medium, *Geophys. J. Int.,* **139**(2), 263–272.

Main, I.G., Leonard, T., Papasouliotis, O., Hatton, C.G. & Meredith, P.G., 1999. One slope or two? detecting statistically significant breaks of slope in geophysical data, with application to fracture scaling relationships, *Geophys. Res. Lett.,* **26**(18), 2801–2804.

Majer, E.L., Baria, R., Stark, M., Oates, S., Bommer, J., Smith, B. & Asanuma, H., 2007. Induced seismicity associated with Enhanced Geothermal Systems, *Geothermics,* **36**(3), 185–222.

Marzocchi, W. & Sandri, L., 2003. A review and new insights on the estimation of the *b*-value and its uncertainty, *Ann. Geophys.,* **46**(6), 1271–1282.

Mavko, G., Mukerji, T. & Dvorkin, J., 2003. *The Rock Physics Handbook: Tools for Seismic Analysis of Porous Media,* Stanford-Cambridge program, Cambridge Univ. Press.

Maxwell, S., 2014. *Microseismic Imaging of Hydraulic Fracturing: Improved Engineering of Unconventional Shale Reservoirs, SEG Distinguished Instructor Series No. 17,* Society of Exploration Geophysicists.

McGarr, A., 1976. Seismic moments and volume changes, *J. geophys. Res.,* **81**(8), 1487–1494.

McGarr, A., 2014. Maximum magnitude earthquakes induced by fluid injection, *J. geophys. Res. Solid Earth,* **119**(2), 1008–1019.

Nur, A. & Booker, J.R., 1972. Aftershocks caused by pore fluid flow? *Science,* **175**(4024), 885–887.

Oppenheimer, D.H., 1986. Extensional tectonics at the Geysers Geothermal Area, California, *J. geophys. Res. Solid Earth,* **91**(B11), 11463–11476.

Parotidis, M., Shapiro, S.A. & Rothert, E., 2004. Back front of seismicity induced after termination of borehole fluid injection, *Geophys. Res. Lett.,* **31**(2), L02612.

Reiter, L., 1991. *Earthquake Hazard Analysis: Issues and Insights,* Columbia University Press.

Roberts, N.S., Bell, A.F. & Main, I.G., 2015. Are volcanic seismic *b*-values high, and if so when? *J. Volcanol. Geotherm. Res.,* **308**, 127–141.

Sammonds, P., Meredith, P. & Main, I., 1992. Role of pore fluids in the generation of seismic precursors to shear fracture, *Nature,* **359**(6392), 228–230.

Schmittbuhl, J., Lengliné, O., Cornet, F., Cuenot, N. & Genter, A., 2014. Induced seismicity in EGS reservoir: the creep route, *Geotherm. Energy,* **2**, 1–13.

Shapiro, S., 2015. *Fluid-Induced Seismicity,* Cambridge University Press.

Shapiro, S.A. & Dinske, C., 2009. Scaling of seismicity induced by nonlinear fluid-rock interaction, *J. geophys. Res. Solid Earth,* **114**(B9), B09307, doi:10.1029/2008JB006145.

Shapiro, S.A., Audigane, P. & Royer, J.J., 1999. Large-scale in situ permeability tensor of rocks from induced microseismicity, *Geophys. J. Int.,* **137**(1), 207–213.

Shapiro, S.A., Dinske, C., Langenbruch, C. & Wenzel, F., 2010. Seismogenic index and magnitude probability of earthquakes induced during reservoir fluid stimulations, *The Leading Edge,* **29**(3), 304–309.

Shi, Y. & Bolt, B., 1982. The standard error of the magnitude-frequency *b*-value, *Bull. seism. Soc. Am.,* **72**(5), 1677–1687.

Verdon, J.P., Stork, A.L., Bissell, R.C., Bond, C.E. & Werner, M.J., 2015. Simulation of seismic events induced by CO2 injection at In Salah, Algeria, *Earth. Planet. Sci. Lett.,* **426,** 118–129.

Zang, A., Oye, V., Jousset, P., Deichmann, N., Gritto, R., McGarr, A., Majer, E. & Bruhn, D., 2014. Analysis of induced seismicity in geothermal reservoirs - an overview, *Geothermics,* **52,** 6–21.